Machine learning accelerated discovery of superconducting two-dimensional Janus transition metal sulfhydrates

Jingyu Li [1,3] Liuming Wei,[2,3] Xianbiao Shi,[1,3] Lanting Shi,[4] Jianguo Si [4] Peng-Fei Liu [1,3,*] and Bao-Tian Wang[1,3,†]

[1]*Institute of High Energy Physics, Chinese Academy of Sciences, Beijing 100049, China*

[2]*Department of Network Security, Henan Police College, Zhengzhou 450046, China*

[3]*Spallation Neutron Source Science Center, Dongguan 523803, China*

[4]*Songshan Lake Materials Laboratory, Dongguan, Guangdong 523808, China*

(Received 3 February 2024; accepted 2 May 2024; published 10 May 2024)

The MoSH monolayer, one of the Janus transition metal sulfhydrates synthesized by stripping the top-layer S of MoS_2 and replacing it with H atoms [Wan *et al.*, ACS Nano **15**, 20319 (2021)], has been predicted to host strong coupling two-gap superconductivity with a calculated critical temperature T_c of about 28.58 K at atmospheric pressure. In this work, by using machine learning aided high-throughput calculations, we narrow down 180 possible configurations of two-dimensional Janus transition metal sulfhydrates (MXH monolayers, where M = transition metal group elements and X = S, Se, and Te) to 20 stable metals. Among them, we identify six low-energy monolayers that are potential high-T_c superconductors. Notably, the 1T-TiSH monolayer stands out with the highest T_c of approximately 48 K, surpassing the superconducting properties of 1H-MoSH (T_c = 28.58 K) and the well-known MgB_2 superconductor (T_c = 39 K). By solving the anisotropic Migdal-Eliashberg equations, we find that 1T-TiSH naturally exhibits a one-gap superconducting nature with strong electron-phonon coupling ($\lambda = 2.79$) originating from the interactions of Ti $d_{xz,yz}$ orbitals and in-plane vibrations, which is different from and better than the 1H-MoSH monolayer ($\lambda = 1.60$). The presented results enrich families of Janus transition metal sulfhydrates and accelerate the design of novel two-dimensional superconductors.

DOI: 10.1103/PhysRevB.109.174516

I. INTRODUCTION

Achieving high-temperature superconductivity remains an enduring scientific challenge in current condensed matter physics and materials science. However, recent advancements in metal hydrides, which exhibit record high-T_c superconductivity, have garnered significant attention due to key advances in the experimental synthesis technique, especially at high pressure [1]. While metallic hydrogen has been theoretically proposed as a promising candidate for achieving high-temperature superconductivity, the metallization of hydrogen requires exceptionally high pressures. Moreover, the significant experimental challenges of synthesizing metallic hydrogen may introduce inaccuracies in the measurement of superconductivity properties [2,3]. As a result, researchers have turned their attention to hydrides as a more accessible and promising path towards achieving high-temperature superconductivity. Recent publications reported record-breaking or potential high-T_c superconductivity in metal hydrides that have been experimentally synthesized, including LaH_{10} [4], ZrH_3 [5], CeH_9 [6], and YH_9 [7]. The above findings have served as strong motivators for exploring various hydride materials. Furthermore, there has been a notable surge in interest in two-dimensional (2D) superconductivity, driven by the discovery of remarkably high critical temperatures [8] and potential applications in quantum technologies [9–11]. These 2D materials are anticipated by the presence of strong electron-phonon interactions and a multigap superconducting nature, such as the hydrogenation of monolayer MgB_2 (T_c = ~67 K) [12], doped graphane (hydrogenated graphene; T_c = ~90 K) [13], and the intrinsic Janus MoSH monolayer (T_c = ~28.58 K) [14,15]. Furthermore, these 2D materials demonstrate high-T_c superconductivity under atmospheric pressure, driven by quantum confinement and surface effects. This sets them apart from their bulk counterparts, which typically require superhigh pressure conditions. Thus, it is of great significance to study the possible high-T_c superconductivity in 2D metal hydrides and hydrogenated 2D materials.

Experimentally, determining the crystal structure and composition of hydrides poses a significant challenge. This complexity arises from the limitations of conventional experimental techniques, such as x-ray diffraction, which is unable to precisely detect the positions of hydrogen atoms [16]. Instead, researchers have turned to rapidly advancing fields of computational materials science, such as density functional theory (DFT), high-throughput computation, and machine learning, to explore and discover metal hydrides exhibiting high-T_c superconductivity. Shipley *et al.* surveyed the landscape of binary hydrides across the entire periodic table from 10 to 500 GPa using the crystal structure prediction method. They found 36 dynamically stable superconductors hydrides with T_c above 100 K by performing high-throughput calculations of T_c based on the predicted crystals [17]. On the basis of the first-principles data of binary hydrogen compounds, Ishikawa *et al.*

*Corresponding author: pfliu@ihep.ac.cn

†Corresponding author: wangbt@ihep.ac.cn

used a materials informatics approach to find hypothetical ternary ones. They predicted $KScH_{12}$, with a superconducting critical temperature of 122 K at 300 GPa, and $GaAsH_6$, with a superconducting critical temperature of 98 K at 180 GPa [18]. Using the crystal structure prediction method, Sun *et al.* searched the high-pressure phase diagram of the Li-*R*-H system and identified the thermodynamically ternary superhydrides Li_2ScH_{20}, Li_2YH_{17}, and Li_2LaH_{17} with high-T_c superconductivity [19]. Recently, Yan *et al.* used first-principles calculations and found 73 2D transition metal hydrides, among which two CuH_2 phases are predicted to have remarkably high T_c of 44.4 and 47.8 K [20]. In these studies, machine learning based approaches have emerged as a powerful new tool for accelerating materials modeling and new materials discovery [21], which allows for the predicted energy, forces, and stresses to closely match those derived from quantum mechanical models [22]. Their efficiency in simulating large systems and ability to carry out multiple tasks within DFT-level accuracy make them ideal for scenarios where DFT's computational demands are prohibitive. Therefore, using rapidly developing machine learning and/or high-throughput strategies, it is possible to expand the family of 2D superconducting hydride materials and explore the possibility of raising their T_c.

Previously, we found that the experimentally synthesized Janus 1*H*-MoSH monolayer is a robust conventional high-temperature two-gap superconductor [15] based on first-principles calculations. In this work, taking the 1*H*-MoSH monolayer as a prototype, we perform machine learning aided first-principles high-throughput calculations for 180 Janus *MX*H monolayers (M = transition metal group elements; X = S, Se, and Te) to expedite the discovery of new and potential high-T_c 2D superconductors. The results show that six low-energy stable monolayers exhibit superconductivity with T_c values exceeding 8 K. Among them, the 1*T*-TiSH monolayer shows the highest intrinsic T_c of 48 K with a strong electron-phonon coupling (EPC) ($\lambda = 2.79$), which arises from Ti $d_{xz,yz}$ orbital driven bands cooperating with soft phonons dominated by Ti's in-plane vibrations. Moreover, the 1*T*-TiSH monolayer is a single-gap superconductor, which is distinct from the multigap MoSH and MgB_2 materials. This verifies that high T_c is independent of the multigap superconducting states.

II. COMPUTATIONAL METHODS

A. Screening materials

Our calculations were completed within the Vienna Ab initio Simulation Package (VASP), using the Perdew-Burke-Ernzerhof exchange-correlation functional under the generalized gradient approximation [23,24]. The plane wave cutoff energy was set to 500 eV. During the geometry optimization, the convergence tolerances for the energy and forces were set to 10^{-6} eV and 0.01 eV/Å, respectively. A $15 \times 15 \times 1$ **k** mesh was sampled in the 2D Brillouin zone. To minimize the interactions between the monolayer and its periodic images, a 20 Å vacuum was used for all calculations.

We employed the PHONOPY code to generate optimal sets of atomic positions to obtain phonon dispersions [25,26]. In this process, a class of machine learning interatomic potentials known as moment tensor potentials (MTPs) were used instead of potentials from VASP in the force calculation step. To calculate MTP forces for the PHONOPY input structures, we utilized a training set consisting of *ab initio* molecular dynamics (AIMD) inputs, along with the MTP training procedure and the integration code [21,27]. The AIMD calculations were performed with a $4 \times 4 \times 1$ supercell via a canonical ensemble using a Nosé -Hoover thermostat.

The enthalpy of formation of Janus *MX*H monolayers was defined as [28]

$$E_{\mathrm{f}} = \{E_{\mathrm{tot}} - (E_{\mathrm{M}} + E_X + E_{\mathrm{H}})\}/3, \tag{1}$$

where E_{tot} is the total energy of the system and E_M, E_X, and E_{H} are the ground state total energies of the elementary crystals of M, X, and H, respectively.

B. EPC and superconductivity

For the identified monolayers, we conducted EPC calculations with the QUANTUM ESPRESSO (QE) package [29,30]. In these calculations, the plane wave basis with a kinetic energy cutoff of 80 Ry was used to simulate the valence electrons, and the ultrasoft pseudopotentials were taken from the library of ultrasoft and projector augmented wave pseudopotentials (PSLIBRARY) [31]. The internal atomic positions were fully relaxed until the force on each atom was smaller than 10 meV/Å. We used a $24 \times 24 \times 1$ **k** mesh with Methfessel-Paxton smearing of 0.02 Ry to complete the self-consistent electron densities. The phonon dispersions were calculated within density functional perturbation theory on a $12 \times 12 \times 1$ **q** mesh using the PHONON module in the QE package. The electron-phonon interpolations for 2D Janus *MX*H monolayers were computed by solving the fully anisotropic Migdal-Eliashberg equations self-consistently [32–34], as implemented in the EPW code [35–37].

The isotropic Eliashberg spectral function $\alpha^2F(\omega)$ was defined as follows:

$$\alpha^2F(\omega) = \frac{1}{N_{\mathbf{F}}N_{\mathbf{k}}N_{\mathbf{q}}} \sum_{\mathbf{k},\mathbf{k}',v} \left|g^v_{\mathbf{k}\mathbf{k}'}\right|^2 \delta(\epsilon_{\mathbf{k}})\delta(\epsilon_{\mathbf{k}'})\delta(\omega - \omega_{\mathbf{q}v}), \tag{2}$$

where $N_{\mathbf{F}}$ is the electronic density of states per spin at the Fermi level, $N_{\mathbf{k}}$ and $N_{\mathbf{q}}$ are the total numbers of **k** and **q** points, $\epsilon_{\mathbf{k}}$ is the Kohn-Sham eigenvalue referred to the Fermi level, and $g^v_{\mathbf{k}\mathbf{k}'}$ is the screened electron-phonon matrix element for the scattering between the electronic states **k** and **k**′ through a phonon with wave vector **q** and frequency $\omega_{\mathbf{q}v}$. According to Eq. (2), the cumulative EPC $\lambda(\omega)$ is given by

$$\lambda(\omega) = 2\int_0^{\omega} d\omega' \alpha^2F(\omega')/\omega', \tag{3}$$

and the momentum-resolved EPC of each electronic state at the Fermi surface associated with a specific phonon mode and wave vector **q** is expressed as

$$\lambda_{\mathbf{k}} = \sum_{\mathbf{k}',v} \delta(\epsilon_{\mathbf{k}'})\left|g^v_{\mathbf{k}\mathbf{k}'}\right|^2/\omega_{\mathbf{q}v}. \tag{4}$$

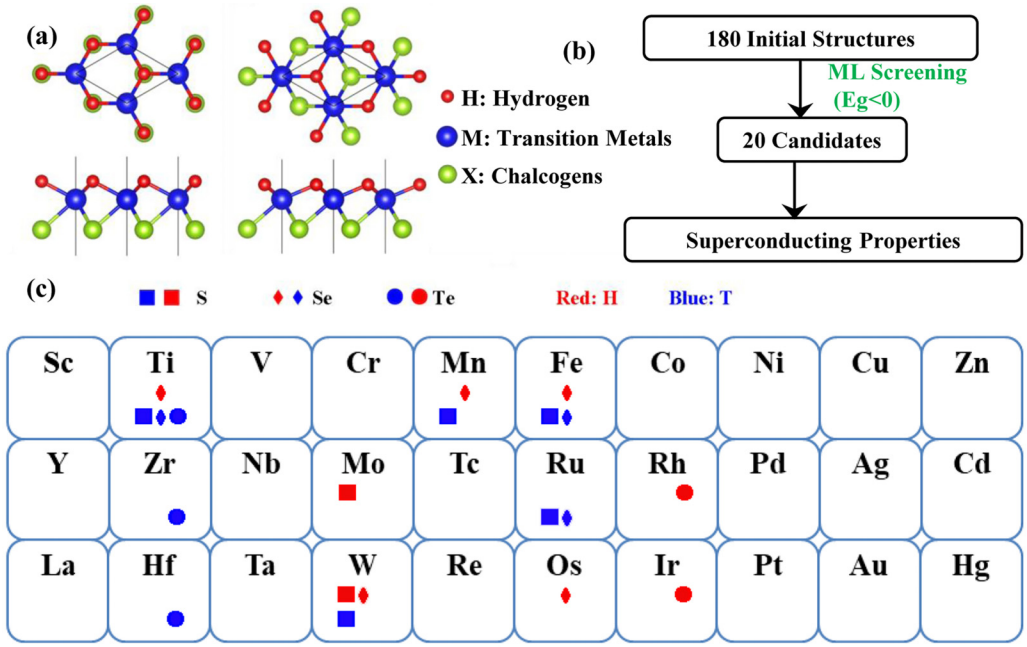

FIG. 1. (a) Top and side views of representative monolayers for 1*H*- and 1*T*-phase *MX*H monolayers. (b) Schematic representation of the fundamental steps to find new 2D stable superconducting Janus transition metal sulfhydrates. (c) The distribution of stable 2D MXH superconducting materials in the periodic table. For clarity, different *X* are represented by different symbols, while distinct 1*H* and 1*T* phases are denoted as different colors.

Then, the anisotropic Migdal-Eliashberg equations are given by

$$Z(\mathbf{k}, i\omega_n) = 1 + \frac{\pi T}{N_F \omega_n} \sum_{\mathbf{k}'n'} \frac{\omega_{n'}}{\sqrt{\omega_{n'}^2 + \Delta^2(\mathbf{k}', i\omega_{n'})}} \times \delta(\epsilon_{\mathbf{k}'}) \lambda(\mathbf{k}, \mathbf{k}', n - n'), \quad (5)$$

and

$$Z(\mathbf{k}, i\omega_n)\Delta(\mathbf{k}, i\omega_n) = \frac{\pi T}{N_F} \sum_{\mathbf{k}'n'} \frac{\Delta(\mathbf{k}', i\omega_{n'})}{\sqrt{\omega_{n'}{}^2 + \Delta^2(\mathbf{k}', i\omega_{n'})}} \times \delta(\epsilon_{\mathbf{k}'})[\lambda(\mathbf{k}, \mathbf{k}', n - n') - \mu_c^*], \quad (6)$$

where $\omega_n = (2n + 1)T$ (n is an integer, and T is the absolute temperature) are Fermion Matsubara frequencies, $Z(\mathbf{k}, i\omega_n)$ is the mass renormalization function, $\Delta(\mathbf{k}, i\omega_n)$ is the superconducting gap function, and $\lambda(\mathbf{k}, \mathbf{k}', n - n')$ is the momentum- and energy-dependent EPC. μ_c^* is the semiempirical Coulomb parameter, which usually is taken between 0.05 and 0.2 for 2D materials [15,38–42]. We used a mean value of $\mu_c^* = 0.1$ here. To solve the anisotropic Migdal-Eliashberg equations for these Janus *MX*H monolayers, an extremely fine interpolated **k** grid of 200 × 200 × 1 and a **q** grid of 200 × 200 × 1 were used. In the Migdal-Eliashberg equations, the frequency cutoff was set to 6 times the maximum phonon frequency. To account for the Dirac δ functions, we applied Lorentzian broadenings of 100 meV for electrons and 0.5 meV for phonons. Additionally, non-self-consistent calculations of the electronic wave functions required for the Wannier Fourier interpolations [43–45] were conducted using a uniform **k** mesh of 24 × 24 × 1.

To reduce computational complexity, we also employed the simplified McMillan-Allen-Dynes formula [46] in the PHONON module within the QE package to quickly determine the superconducting transition temperature T_c, which was defined as follows:

$$T_c = \frac{\omega_{\log}}{1.2} \exp\left[\frac{-1.04(1 + \lambda)}{\lambda(1 - 0.62\mu^*) - \mu^*}\right], \quad (7)$$

were $\omega_{\log}$ and λ are the logarithmic average frequency and EPC constant, respectively. μ^* is the semiempirical Coulomb parameter, and it is set to 0.1 in this work.

III. RESULTS AND DISCUSSION

A. Screening stable candidates

We previously constructed a stable hexagonal 1*H*-MoSH monolayer with the closely packed sandwich structure, that is, the top-layer sulfur atoms in the MoS_2 monolayer can be replaced with hydrogen atoms [15]. In this work, we examine two types of phases for each constituent, namely, the 1*H* and 1*T* phases for the hexagonal *MX*H monolayers, where *M* represents elements from the transition metal groups and *X* stands for S, Se, and Te, as illustrated in Fig. 1(a). As a result, there are 180 possible configurations for all combinations. We further investigate their stability by performing machine learning aided high-throughput phonon calculations. We find that 57 configurations are dynamically stable, and 20 of them are metals [see Figs. 1(b) and 1(c) and Figs. S1– S3 in the Supplemental Material [47]). Notably, among them, the 1*H*-MoSH monolayer was recently experimentally synthesized as an intermediate by substituting the top layer S of MoS_2 with H atoms through gentle H_2 plasma treatment at room temperature [48,49]. Taking 1*H*-MoSH as a benchmark, we select six candidates (1*H*-TiSeH, 1*T*-TiSH, 1*T*-TiSeH, 1*T*-TiTeH, 1*T*-ZrTeH, and 1*T*-HfTeH) as high-T_c 2D superconductors

TABLE I. The calculated superconducting properties for several candidates, including the total EPC constant λ, the density of the electronic states N_F (in states per spin per rydberg per unit cell), the logarithmic-average phonon frequency $\omega_{\log}$ (in K), and the estimated critical temperatures T_c (in K). These data were obtained by solving the semiempirical McMillan-Allen-Dynes formulas using the PHONON module within the QE package.

Structures	λ	N_F	$\omega_{\log}$	T_c
1*H*-TiSeH	1.43	2.50	119.90	13.09
1*H*-MoSH	1.48	8.47	178.36	20.07
1*T*-TiSH	2.71	3.77	175.80	30.19
1*T*-TiSeH	1.44	2.75	166.70	18.30
1*T*-TiTeH	1.45	2.60	120.92	13.31
1*T*-ZrTeH	1.18	1.81	103.10	9.04
1*T*-HfTeH	1.29	1.68	81.98	7.96

with low formation energies, making them feasible for experimental realization (see Supplemental Material, Table S1). Meanwhile, these stable sheets hold high T_c values evaluated by the simplified McMillan-Allen-Dynes formula. The calculated superconducting parameters, including the total EPC constant λ, the logarithmic average phonon frequency $\omega_{\log}$, the density of the electronic states N_F, and the superconducting transition temperature T_c, are listed in Table I. Clearly, the 1*T*-TiSH monolayer stands out, with a remarkable T_c value of approximately 29.26 K, which is 65% higher than that of the Janus 1*H*-MoSH monolayer, as shown in Fig. 2. The EPC constant λ for the Janus 1*T*-TiSH monolayer is exceptionally high at 2.79, significantly surpassing the values of other candidates. The high λ value is likely due to the substantial electron participation at the Fermi level (indicated by the large N_F) and a high average phonon frequency $\omega_{\log}$, which make strong contributions to the formation of superconducting Cooper pairs. Subsequently, we mainly discuss the electron structure, phonon dispersion, and electron-phonon coupling of 1*T*-TiSH with the highest T_c value.

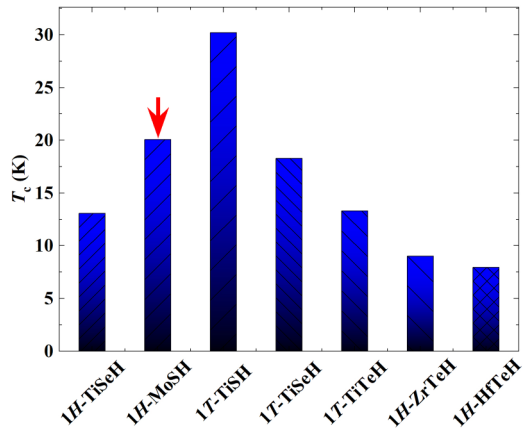

FIG. 2. Superconducting transition temperature T_c for the selective candidates. The red arrow represents 1*H*-phase MoSH material that has been synthesized in experiment. These data are obtained by solving the semiempirical McMillan-Allen-Dynes formulas using the PHONON module within the QE package.

B. Electronic and phonon band structures

To explore the origins of the significant EPC constant and high superconducting transition temperature T_c observed in the 1*T*-TiSH monolayer, we conduct calculations on its electronic and phononic structures. The calculated orbital-resolved band structure, partial electronic density of states (DOS), and Fermi surfaces of the Janus 1*T*-TiSH monolayer are presented in Fig. 3(a). Overall, its band structure is metallic, with the valence band (VB) crossing the Fermi level, which is similar to the band structure of the Janus 1*H*-MoSH monolayer [15]. Since Ti atoms ($3d^24s^2$) have fewer valence electrons than Mo atoms ($4d^55s^1$), the band structure of 1*T*-TiSH is akin to the hole-doped electronic structure of 1*H*-MoSH. Thus, the isolated VB shifts upward and crosses the Fermi level for 1*T*-TiSH. Due to the existence of the flattened band around the *K* point, 1*T*-TiSH has heavy fermions and a Van Hove singularity in the vicinity of the Fermi level [50,51]. The heavy band with the Van Hove singularity contributes to a high electron density at the Fermi level (5.15 states/(spin/Ry) per unit cell). It favors the formation of high-T_c electron-phonon superconductors, which is different from semiconducting the 1*T*-TiS_2 monolayer, as discussed in the Supplemental Material [47,52,53]. In analogy to the Janus 1*H*-MoSH monolayer, the orbitals in the 1*T*-TiSH monolayer primarily originate from the Ti *d* orbitals, with small contributions from the S *p* orbitals, while the contributions of the H *s* orbitals can be neglected at the Fermi level. Since the crystal belongs to point group C_{3v}, the Ti *d* orbitals can be classified into three categories: A_{1g} (d_{z^2}), E_{2g} (d_{xy,x^2-y^2}), and E_{1g} ($d_{xz,yz}$). The presence of broken out-of-plane symmetry in the Janus 1*T*-TiSH monolayer allows for hybridization among these three categories. Specifically, the Ti d_{z^2} orbitals dominate the isolated band around the Γ point, while the $d_{xz,yz}$ orbitals mainly contribute to the band near the *K* point. Away from the high-symmetry points, the band is primarily derived by the Ti d_{xy,x^2-y^2} orbitals. There are two crossing points between the VB and the Fermi energy, which divides the Fermi surfaces of the Janus 1*T*-TiSH monolayer into two concentric regions around the Γ point in the right panel of Fig. 3(a). The inner region features a six-petal-like hole pocket originating from the Ti d_{xy,x^2-y^2} orbitals. In contrast, the outer region exhibits a conduit-shaped hole pocket dominated by the Ti $d_{xz,yz}$ states. The coloration on the Fermi surfaces represents the relative Fermi velocities v_F with anisotropy.

Figure 3(b) illustrates the phonon dispersions and the projected phonon density of states (PDOS) for the Janus 1*T*-TiSH monolayer across the entire frequency range. With the primitive cell containing three atoms, there are a total of nine phonon modes: three acoustic and six optical branches. The absence of unstable modes in any of the phonon branches provides strong evidence of the dynamic stability of the Janus 1*T*-TiSH monolayer. In the lowest-energy acoustic branch, noticeable phonon softening is observed along the Γ-*K* path, primarily originating from the in-plane vibrations of the Ti atoms. The high-frequency contributions above 60 meV are predominantly due to vibrations of the H atoms, while the low-energy region comprises three acoustic and optic phonon branches, with the primary contributions coming from the vibrations of Ti and S atoms. It is worth noting that the

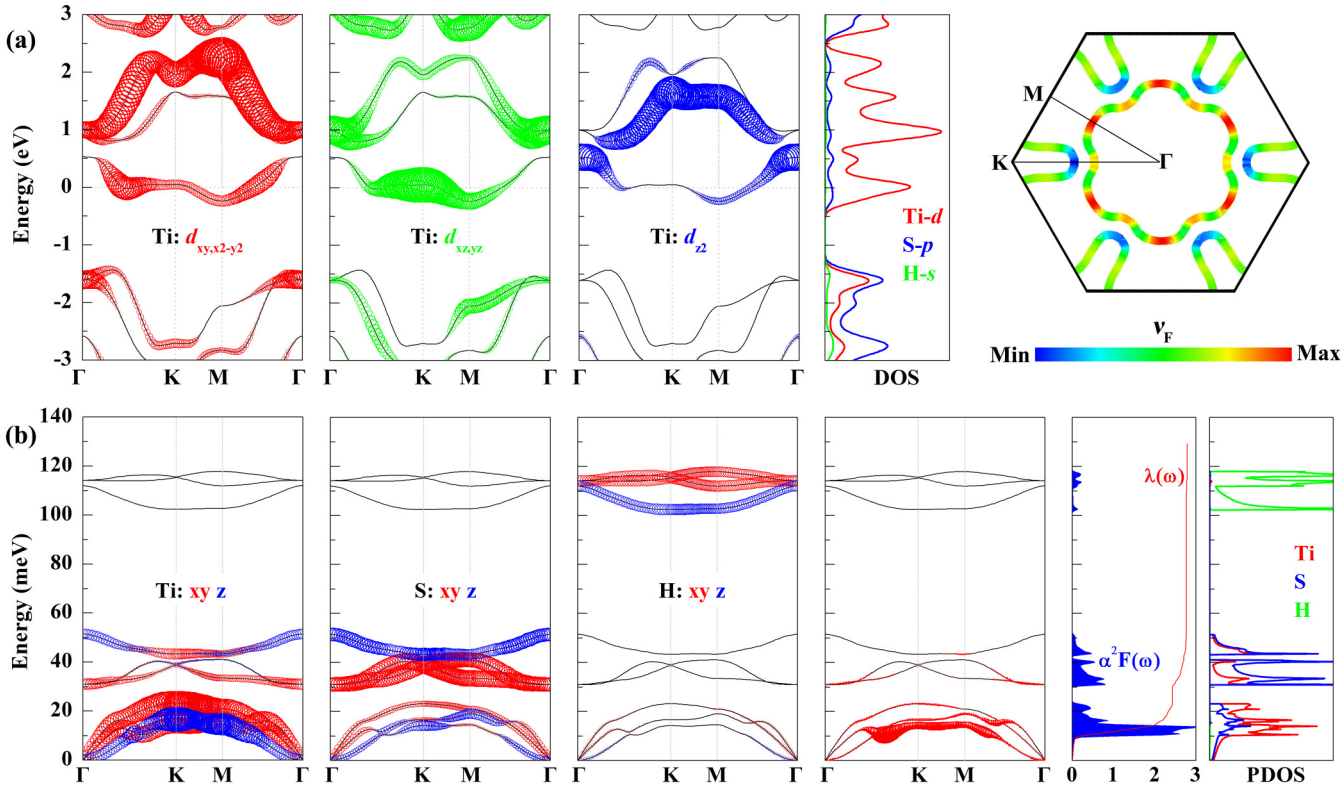

FIG. 3. (a) Calculated orbital-resolved band structures, partial electronic density of states (DOS), and Fermi surfaces of the Janus 1*T*-TiSH monolayer. The red, green, and blue circles highlight the bands arising from Ti d_{xy,x^2-y^2}, $d_{xz,yz}$, and d_{z^2} orbitals, respectively. The 2D Fermi surfaces are colored according to the relative Fermi velocity. The red, green, and blue regions have high, medium, and low Fermi velocities v_F, respectively. (b) Phonon dispersion highlighting the primary nature of the different modes and Eliashberg function $\alpha^2F(\omega)$ with $\lambda(\omega)$ of the Janus 1*T*-TiSH monolayer. The in-plane and out-of-plane vibrations are shown by red and blue circles. The red, blue, and green lines in the PDOS plot represent the contributions of Ti, S, and H atoms, respectively.

frequencies of the entire optical modes resulting from H atom vibrations fall within the range of 100 to 120 meV, which differs from those of the hydrogenated MoSH monolayer (ranging from 87 to 131 meV) [15]. This discrepancy can be attributed to the shorter thickness ($d = 2.34$ Å) and stronger interaction in the 1*T*-TiSH monolayer compared to the 1*H*-MoSH ($d = 2.65$ Å) monolayer. It accompanies suppressed vibrations along the z direction and coupled in-plane vibrations in the phonon dispersion. These findings further support that our predicted T_c of the Janus 1*T*-TiSH monolayer should be significantly distinct from and possibly higher than that of the Janus 1*H*-MoSH metal hydrides.

C. Electron-phonon interactions

Significant Van Hove singularities appear near the Fermi level in the band structure, while pronounced Kohn anomalies emerge along the Γ-*K* path in the low-energy acoustic mode (as seen in Fig. 3). These features suggest the potential for a strong EPC. Thus, we now turn to a discussion of the electron-phonon Eliashberg spectral function $\alpha^2F(\omega)$, which reflects the intensity of the EPC. From the calculated $\alpha^2F(\omega)$ in Fig. 3(b), we observe a couple of prominent peaks below 30 meV, corresponding to soft modes along the Γ-*K* direction and a relatively flat phonon dispersion along the *M*-*K* direction. These characteristics primarily originate from the in-plane vibrations of the Ti atoms. Remarkably, they account for approximately 87.10% of the total EPC strength of $\lambda = 2.43$. The strong EPC is in favor of strong electron-phonon superconductivity. Obviously, $\alpha^2F(\omega)$ and the PDOS can be divided into three regions: the low-frequency acoustic branches are dominated by the vibrations of Ti atoms, while the medium- and high-frequency optical branches are influenced by the vibrations of S and H atoms, respectively. Overall, we can conclude that the EPC in the Janus 1*T*-TiSH monolayer is primarily governed by in-plane Ti atomic vibrations. This is evident from the fact that the low-energy optical phonons contribute only about 11.50% to the total λ, while the higher-frequency region accounts for approximately 1.4% of the total λ. It is worth noting that this EPC behavior differs from many other hydride superconductors, such as LaH_{10}, in which high-frequency optical phonon modes of H vibrations contribute 82% of λ [54]. Combined with our understanding of the electronic band structure, we can conclude that the superconductivity in the Janus 1*T*-TiSH monolayer mainly originates from the in-plane Ti atomic vibrations strongly coupled with its $3d_{xy,x^2-y^2}$ and $3d_{xz,yz}$ states.

The mode-resolved EPC λ_{qv}, as calculated by Eq. (4), is visually represented in Fig. 4. Clearly, the EPC mainly comes from three acoustic modes, with visible contributions from the two lowest optical phonons, while the high-frequency vibrational modes have negligible impact. These results agree well

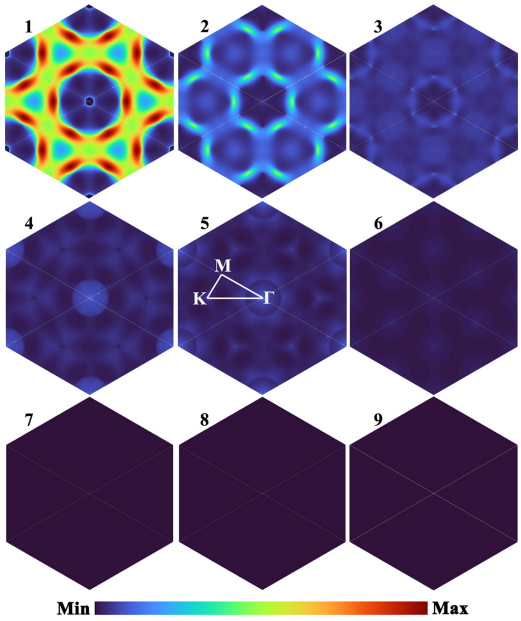

FIG. 4. The mode-resolved EPC λ_{qv} distributions in the Brillouin zone for the Janus 1*T*-TiSH monolayer. The number of each mode is shown in the top left corner of each plot. The colors represent the size of λ_{qv}, in which the red, green, and blue regions have high, medium, and low values of λ_{qv}, respectively.

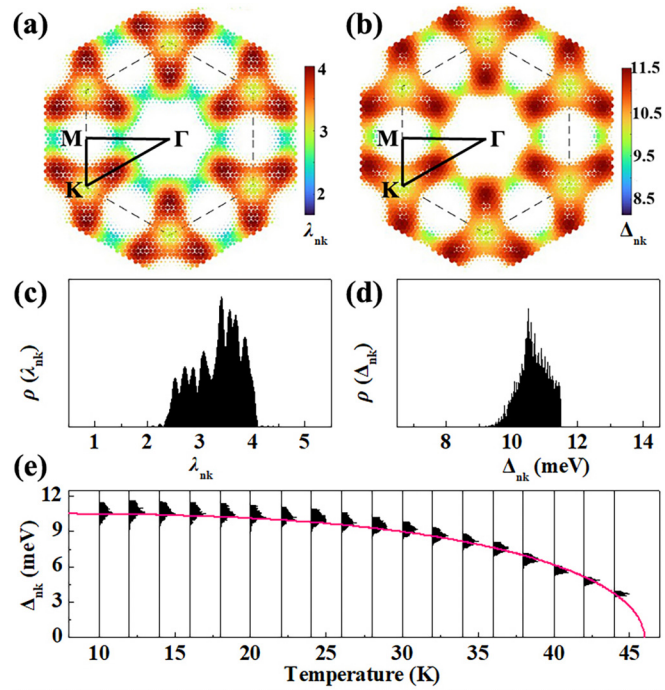

FIG. 5. EPC parameters $\lambda_{n\mathbf{k}}$ and superconducting gaps $\Delta_{n\mathbf{k}}$ for the Janus 1*T*-TiSH monolayer. (a) Momentum-resolved EPC parameters $\lambda_{n\mathbf{k}}$ on the Fermi surfaces, with the (c) normalized distribution strength $\rho(\lambda)$ of the EPC parameters $\lambda_{n\mathbf{k}}$. (b) Momentum-resolved superconducting gaps $\Delta_{n\mathbf{k}}$ at 10 K on the Fermi surfaces, with the (d) normalized distribution strength $\rho(\Delta_{nk})$ of the superconducting gaps $\Delta_{n\mathbf{k}}$ at 10 K. (e) Histograms of the temperature-dependent superconducting gap $\Delta_{n\mathbf{k}}$ for the electronic states around the Fermi level. The red line is the BCS fit to the calculated data, which serves as a guide to the eye.

with our above analysis based upon Fig. 3(b). As phonon frequencies increase, the contributions to the EPC progressively decrease. The first acoustic phonon branch, contributing the most to the EPC, exhibits the highest values of λ along the Γ-*K* path, forming a discontinuous triangular ring around the *K* point in Fig. 3(b). This indicates that the largest EPC values primarily originate from the previously mentioned Kohn anomalies. Obviously, the Kohn anomaly phonon near the *K* point makes larger contributions than that near the *M* point. This behavior is similar to that observed in the 1*H*-MoSH monolayer, where the softened modes in the low-energy acoustic phonons exhibit very large λ_{qv}. The λ_{qv} distributions for the second acoustic phonon branch in the Janus 1*T*-TiSH monolayer are characterized by a weak discontinuous triangular ring around either the *K* or *M* point. The contributions to λ_{qv} from the third to fifth phonon branches are relatively small. Starting in the sixth to ninth phonon modes, λ_{qv} contributions become nearly nonexistent within the Brillouin zone. Overall, the dominant contributor to the EPC in the Janus 1*T*-TiSH monolayer is the lowest acoustic phonon branch, which is similar to the behavior observed in the 1*H*-MoSH monolayer [15]. However, this differs from the EPC behavior in the hydrogenated MgB_2 monolayer [12] and in materials like LaH_{10} [54] and H_3S [55], where optical phonon vibrations from hydrogen contribute the most to λ.

D. Anisotropic superconductivity

To comprehensively describe the anisotropic superconductivity of the Janus 1*T*-TiSH monolayer, we undertake the self-consistent solution of the Migdal-Eliashberg equations. In Fig. 5(a), we present the Fermi surface weighted by the momentum-resolved EPC strength $\lambda_{n\mathbf{k}}$, illustrating a slight anisotropic contribution of the Fermi surface electronic states to the EPC. The most significant EPC, with a value of λ = 4.05, is observed along the Γ-*K* line, which is mainly due to the strong coupling between Ti $d_{xz,yz}$ states and the in-plane vibrational modes of the Ti atoms. The normalized distribution $\rho(\lambda)$ of λ in Fig. 5(c) reveals that λ falls within the range of 2.25 to 4.05, with no distinct separation in the $\rho(\lambda)$ distribution. The superconducting gaps $\Delta_{n\mathbf{k}}$ at 10 K, as displayed in Fig. 5(b), are primarily located around the *K* point on the Fermi surfaces. These gaps exhibit a maximum value of 11.5 meV and a minimum of 9.2 meV, indicating weak anisotropy (21%). Similar to the EPC, there is only one peak in the distribution of $\rho(\Delta_{nk})$, as shown in Fig. 5(d). The absence of EPC separation in the $\rho(\Delta_{nk})$ distribution signifies that the Janus 1*T*-TiSH monolayer is a single-gap superconductor, despite possessing two sheets of the Fermi surface. This observation is reasonable because the Janus 1*T*-TiSH monolayer has one band that crosses the Fermi level without significantly different orbital contributions, which would be necessary for the formation of multiple energy gaps. This feature distinguishes it from materials like MgB_2 and the 1*H*-MoSH monolayer, where Fermi surfaces result from different orbitals, leading to distinct superconducting gaps. Furthermore, Fig. 5(e) illustrates the distribution of superconducting gaps $\Delta_{n\mathbf{k}}$ as a function of temperature.

With increasing temperature, the superconducting energy gap gradually diminishes and eventually vanishes at 48 K. This temperature is approximately 2 times higher than that of the 1*H*-MoSH monolayer. While this critical temperature T_c is smaller than that of the hydrogenated monolayer MgB_2 ($T_c = 67$ K, $\lambda = 1.46$) [12], it is close to that of the *t*-CuH_2 monolayer ($T_c \sim 44.4$ K, $\lambda = 1.20$) [20].

IV. SUMMARY AND CONCLUSIONS

In summary, on the basis of machine learning accelerated high-throughput first-principles calculations, we identified six promising candidate materials (1*H*-TiSeH, 1*T*-TiSH, 1*T*-TiSeH, 1*T*-TiTeH, 1*T*-ZrTeH, and 1*T*-HfTeH) within the family of Janus transition metal sulfhydrates which exhibit high T_c values exceeding 8 K. Notably, the Janus 1*T*-TiSH monolayer stands out, with an exceptionally high predicted T_c of 48 K. This remarkable T_c is attributed to the Ti $d_{xz,yz}$ electrons, which exhibit strong coupling with the soft phonons arising from the in-plane vibrations of Ti atoms. This coupling drives the Janus 1*T*-TiSH monolayer into a high-T_c superconducting phase, characterized by a substantial EPC at ambient pressure. Our findings hold significant implications for both theoretical and experimental research in the quest for high-T_c superconductivity within 2D transition metal dichalcogenides and related Janus systems.

ACKNOWLEDGMENTS

The authors acknowledge the financial support from the National Natural Science Foundation of China (Grants No. 12104458, No. 12304095, No. 12204482, No. U2330104, and No.12074381) and the Guangdong Basic and Applied Basic Research Foundation (Grants No. 2023A1515111190, No. 2023A1515110410, No. 2022A1515140030, No. 2022A1515110404, and No. 2021A1515110587). The numerical calculations were performed at the CSNS Scientific Computing Platform of the Institute of High Energy Physics of CAS and the GBA Subcenter of the National HEP Science Data Center.

[1] A. P. Drozdov, M. I. Eremets, I. A. Troyan, V. Ksenofontov, and S. I. Shylin, Conventional superconductivity at 203 kelvin at high pressures in the sulfur hydride system, Nature (London) **525**, 73 (2015).

[2] P. Dalladay-Simpson, R. T. Howie, and E. Gregoryanz, Evidence for a new phase of dense hydrogen above 325 gigapascals, Nature (London) **529**, 63 (2016).

[3] P. Loubeyre, F. Occelli, and P. Dumas, Synchrotron infrared spectroscopic evidence of the probable transition to metal hydrogen, Nature (London) **577**, 631 (2020).

[4] A. P. Drozdov, P. P. Kong, V. S. Minkov, S. P. Besedin, M. A. Kuzovnikov, S. Mozaffari, L. Balicas, F. F. Balakirev, D. E. Graf, V. B. Prakapenka, E. Greenberg, D. A. Knyazev, M. Tkacz, and M. I. Eremets, Superconductivity at 250 K in lanthanum hydride under high pressures, Nature (London) **569**, 528 (2019).

[5] M. A. Kuzovnikov, V. E. Antonov, V. I. Kulakov, V. D. Muzalevsky, N. S. Orlov, A. V. Palnichenko, and Y. M. Shulga, Synthesis of superconducting hcp-ZrH_3 under high hydrogen pressure, Phys. Rev. Mater. **7**, 024803 (2023).

[6] W. Chen, D. V. Semenok, X. Huang, H. Shu, X. Li, D. Duan, T. Cui, and A. R. Oganov, High-temperature superconducting phases in cerium superhydride with a T_c up to 115 K below a pressure of 1 megabar, Phys. Rev. Lett. **127**, 117001 (2021).

[7] P. Kong, V. S. Minkov, M. A. Kuzovnikov, A. P. Drozdov, S. P. Besedin, S. Mozaffari, L. Balicas, F. F. Balakirev, V. B. Prakapenka, S. Chariton, D. A. Knyazev, E. Greenberg, and M. I. Eremets, Superconductivity up to 243 K in the yttrium-hydrogen system under high pressure, Nat. Commun. **12**, 5075 (2021).

[8] J.-F. Ge, Z.-L. Liu, C. Liu, C.-L. Gao, D. Qian, Q.-K. Xue, Y. Liu, and J.-F. Jia, Superconductivity above 100 K in single-layer FeSe films on doped $SrTiO_3$, Nat. Mater. **14**, 285 (2015).

[9] S. Krastanov, H. Raniwala, J. Holzgrafe, K. Jacobs, M. Lončar, M. J. Reagor, and D. R. Englund, Optically heralded entanglement of superconducting systems in quantum networks, Phys. Rev. Lett. **127**, 040503 (2021).

[10] J. Li *et al.*, Printable two-dimensional superconducting monolayers, Nat. Mater. **20**, 181 (2021).

[11] Y. Saito, T. Nojima, and Y. Iwasa, Highly crystalline 2D superconductors, Nat. Rev. Mater. **2**, 16094 (2016).

[12] J. Bekaert, M. Petrov, A. Aperis, P. M. Oppeneer, and M. V. Milošević, Hydrogen-induced high-temperature superconductivity in two-dimensional materials: The example of hydrogenated monolayer MgB_2, Phys. Rev. Lett. **123**, 077001 (2019).

[13] G. Savini, A. C. Ferrari, and F. Giustino, First-principles prediction of doped graphane as a high-temperature electron-phonon superconductor, Phys. Rev. Lett. **105**, 037002 (2010).

[14] R. Ku, L. Yan, J.-G. Si, S. Zhu, B.-T. Wang, Y. Wei, K. Pang, W. Li, and L. Zhou, *Ab initio* investigation of charge density wave and superconductivity in two-dimensional Janus $2H/1T$-MoSH monolayers, Phys. Rev. B **107**, 064508 (2023).

[15] P.-F. Liu, F. Zheng, J. Li, J.-G. Si, L. Wei, J. Zhang, and B.-T. Wang, Two-gap superconductivity in a Janus MoSH monolayer, Phys. Rev. B **105**, 245420 (2022).

[16] M. Einaga, M. Sakata, T. Ishikawa, K. Shimizu, M. I. Eremets, A. P. Drozdov, I. A. Troyan, N. Hirao, and Y. Ohishi, Crystal structure of the superconducting phase of sulfur hydride, Nat. Phys. **12**, 835 (2016).

[17] A. M. Shipley, M. J. Hutcheon, R. J. Needs, and C. J. Pickard, High-throughput discovery of high-temperature conventional superconductors, Phys. Rev. B **104**, 054501 (2021).

[18] T. Ishikawa, T. Miyake, and K. Shimizu, Materials informatics based on evolutionary algorithms: Application to search for superconducting hydrogen compounds, Phys. Rev. B **100**, 174506 (2019).

[19] Y. Sun, Y. Wang, X. Zhong, Yu Xie, and H. Liu, High-temperature superconducting ternary Li-*R*-H superhydrides at high pressures (R = Sc, Y, La), Phys. Rev. B **106**, 024519 (2022).

[20] X. Yan, S. Ding, X. Zhang, A. Bergara, Y. Liu, Y. Wang, X.-F. Zhou, and G. Yang, Enhanced superconductivity in CuH_2 monolayers, Phys. Rev. B **106**, 014514 (2022).

[21] B. Mortazavi, I. S. Novikov, E. V. Podryabinkin, S. Roche, T. Rabczuk, A. V. Shapeev, and X. Zhuang, Exploring phononic properties of two-dimensional materials using machine learning interatomic potentials, Appl. Mater. Today **20**, 100685 (2020).

[22] A. V. Shapeev, Moment tensor potentials: A class of systematically improvable interatomic potentials, Multiscale Model. Simul. **14**, 1153 (2016).

[23] G. Kresse and J. Furthmüller, Efficient iterative schemes for *ab initio* total-energy calculations using a plane-wave basis set, Phys. Rev. B **54**, 11169 (1996).

[24] G. Kresse and D. Joubert, From ultrasoft pseudopotentials to the projector augmented-wave method, Phys. Rev. B **59**, 1758 (1999).

[25] A. Togo, L. Chaput, T. Tadano, and I. Tanaka, Implementation strategies in phonopy and phono3py, J. Phys.: Condens. Matter **35**, 353001 (2023).

[26] A. Togo, First-principles phonon calculations with phonopy and phono3py, J. Phys. Soc. Jpn. **92**, 012001 (2023).

[27] B. Mortazavi, X. Zhuang, T. Rabczuk, and A. V. Shapeev, Atomistic modeling of the mechanical properties: The rise of machine learning interatomic potentials, Mater. Horiz. **10**, 1956 (2023).

[28] L. Wang, Y. Shi, M. Liu, A. Zhang, Y.-L. Hong, R. Li, Q. Gao, M. Chen, W. Ren, H.-M. Cheng, Y. Li, and X.-Q. Chen, Intercalated architecture of MA_2Z_4 family layered van der Waals materials with emerging topological, magnetic and superconducting properties, Nat. Commun. **12**, 2361 (2021).

[29] P. Giannozzi *et al.*, Quantum ESPRESSO: A modular and open-source software project for quantum simulations of materials, J. Phys.: Condens. Matter **21**, 395502 (2009).

[30] P. Giannozzi, Jr. *et al.*, Advanced capabilities for materials modelling with Quantum ESPRESSO, J. Phys.: Condens. Matter **29**, 465901 (2017).

[31] K. Lejaeghere *et al.*, Reproducibility in density functional theory calculations of solids, Science **351**, aad3000 (2016).

[32] J. Bardeen and D. Pines, Electron-phonon interaction in metals, Phys. Rev. **99**, 1140 (1955).

[33] F. Giustino, Electron-phonon interactions from first principles, Rev. Mod. Phys. **89**, 015003 (2017).

[34] E. R. Margine and F. Giustino, Anisotropic Migdal-Eliashberg theory using Wannier functions, Phys. Rev. B **87**, 024505 (2013).

[35] F. Giustino, M. L. Cohen, and S. G. Louie, Electron-phonon interaction using Wannier functions, Phys. Rev. B **76**, 165108 (2007).

[36] J. Noffsinger, F. Giustino, B. D. Malone, C.-H. Park, S. G. Louie, and M. L. Cohen, EPW: A program for calculating the electron–phonon coupling using maximally localized Wannier functions, Comput. Phys. Commun. **181**, 2140 (2010).

[37] S. Poncé, E. R. Margine, C. Verdi, and F. Giustino, EPW: Electron–phonon coupling, transport and superconducting properties using maximally localized Wannier functions, Comput. Phys. Commun. **209**, 116 (2016).

[38] J.-Y. You, B. Gu, G. Su, and Y. P. Feng, Two-dimensional topological superconductivity candidate in a van der Waals layered material, Phys. Rev. B **103**, 104503 (2021).

[39] W.-H. Dong, Y.-Y. Zhang, Y.-F. Zhang, J.-T. Sun, F. Liu, and S. Du, Superconductivity and topological aspects of two-dimensional transition-metal monohalides, npj Comput. Mater. **8**, 185 (2022).

[40] Y. Zhao, S. Zeng, C. Lian, Z. Dai, S. Meng, and J. Ni, Multigap anisotropic superconductivity in borophenes, Phys. Rev. B **98**, 134514 (2018).

[41] S. Singh, A. H. Romero, J. D. Mella, V. Eremeev, E. Muñoz, A. N. Alexandrova, K. M. Rabe, D. Vanderbilt, and F. Muñoz, High-temperature phonon-mediated superconductivity in monolayer $Mg_2B_4C_2$, npj Quantum Mater. **7**, 37 (2022).

[42] P.-F. Liu, J. Li, X.-H. Tu, H. Yin, B. Sa, J. Zhang, D. J. Singh, and B.-T. Wang, Prediction of superconductivity and topological aspects in single-layer β-Bi_2Pd, Phys. Rev. B **102**, 155406 (2020).

[43] N. Marzari, A. A. Mostofi, J. R. Yates, I. Souza, and D. Vanderbilt, Maximally localized Wannier functions: Theory and applications, Rev. Mod. Phys. **84**, 1419 (2012).

[44] A. A. Mostofi, J. R. Yates, G. Pizzi, Y.-S. Lee, I. Souza, D. Vanderbilt, and N. Marzari, An updated version of wannier90: A tool for obtaining maximally-localised Wannier functions, Comput. Phys. Commun. **185**, 2309 (2014).

[45] G. Pizzi *et al.*, Wannier90 as a community code: New features and applications, J. Phys.: Condens. Matter **32**, 165902 (2020).

[46] W. L. McMillan, Transition temperature of strong-coupled superconductors, Phys. Rev. **167**, 331 (1968).

[47] See Supplemental Material at http://link.aps.org/supplemental/10.1103/PhysRevB.109.174516 for the contrast between 1T-TiS2 and 1T-TiSH monolayers (Sec. 1), calculated phonon dispersions of 20 possible metallic monolayers in Fig. S1 and S2, calculated band structures, density of states, mode-resolved phonon dispersions and Eliashberg function $\alpha^2F(\omega)$ of 6 potential high-T_c monolayer superconductors (1H-TiSeH, 1H-MoSH, 1T-TiSeH, 1T-TiTeH, 1T-ZrTeH, and 1T-HfTeH) in Fig. S3 and S4. Table S1 shows the lattice constants, bond lengths, and formation energy of 20 possible metallic monolayers, and which includes Refs. [52,53].

[48] X. Wan, E. Chen, J. Yao, M. Gao, X. Miao, S. Wang, Y. Gu, S. Xiao, R. Zhan, K. Chen, Z. Chen, X. Zeng, X. Gu, and J. Xu, Synthesis and characterization of metallic Janus MoSH monolayer, ACS Nano **15**, 20319 (2021).

[49] A.-Y. Lu, H. Zhu, J. Xiao, C.-P. Chuu, Y. Han, M.-H. Chiu, C.-C. Cheng, C.-W. Yang, K.-H. Wei, Y. Yang, Y. Wang, D. Sokaras, D. Nordlund, P. Yang, D. A. Muller, M.-Y. Chou, X. Zhang, and L.-J. Li, Janus monolayers of transition metal dichalcogenides, Nat. Nanotechnol. **12**, 744 (2017).

[50] L.-T. Shi, J.-G. Si, A. Liang, R. Turnbull, P.-F. Liu, and B.-T. Wang, Topological and superconducting properties in bilayer kagome metals YT_6Sn_6 (T = V, Nb, Ta), Phys. Rev. B **107**, 184503 (2023).

[51] J.-G. Si, L.-T. Shi, P.-F. Liu, P. Zhang, and B.-T. Wang, Superconductivity and topological properties in the kagome metals CsM_3Te_5 (M = Ti, Zr, Hf): A first-principles investigation, Phys. Rev. B **106**, 214527 (2022).

[52] Z. Zhu, Y. Cheng, and U. Schwingenschlögl, Topological phase diagrams of bulk and monolayer $TiS_{2-x}Te_x$, Phys. Rev. Lett. **110**, 077202 (2013).

[53] J.-H. Liao, Y.-C. Zhao, Y.-J. Zhao, X.-B. Yang, and Y. Chen, Doping induced charge density wave in monolayer TiS_2 and phonon-mediated superconductivity, J. Appl. Phys. **127**, 044301 (2020).

[54] L. Liu, C. Wang, S. Yi, K. W. Kim, J. Kim, and J.-H. Cho, Microscopic mechanism of room-temperature superconductivity in compressed LaH_{10}, Phys. Rev. B **99**, 140501(R) (2019).

[55] D. Duan, Y. Liu, F. Tian, D. Li, X. Huang, Z. Zhao, H. Yu, B. Liu, W. Tian, and T. Cui, Pressure-induced metallization of dense $(H_2S)_2H_2$ with high-T_c superconductivity, Sci. Rep. **4**, 6968 (2014).